Numerical Simulation of Grid-Generated Turbulence Interaction with a NACA0012 Airfoil

AIAA AVIATION Forum
12-16 June 2023, San Diego, CA and Online
AIAA AVIATION 2023 Forum

10.2514/6.2023-3633

Numerical Simulation of Grid-Generated Turbulence Interaction with a NACA0012 Airfoil

Leone Trascinelli* and Luke Bowen†
Faculty of Engineering, University of Bristol, BS8 1TR, Bristol, United Kingdom

Andrea Piccolo‡, Riccardo Zamponi§ and Daniele Ragni¶
Delft University of Technology, 2629HS, Delft, The Netherlands

Francesco Avallone‖
Politecnico di Torino, Corso Duca degli Abruzzi 24, 10129, Tornio, Italy

Beckett Y. Zhou** and Bin Zang††
Faculty of Engineering, University of Bristol, BS8 1TR, Bristol, United Kingdom

The present study assesses the ability to numerically predict turbulence-interaction noise of a NACA0012 airfoil with grid-generated turbulence by utilizing the Lattice Boltzmann solver PowerFLOW. Both the near-field flow characteristics and far field noise are bench-marked against an existing experimental study. The grid was chosen to match that from the experiment to provide evidence that the present numerical approach in physically placing a grid upstream of the airfoil can reproduce the turbulence characteristics observed from the benchmark experiment and thus accurately capture the turbulence-interaction noise generated. The comparison of the results show that the turbulence statistics, including turbulence intensity, integral length scales and anisotropy are highly consistent with the experiment. Moreover, far field acoustics of the turbulence interaction as well as the near-field flow properties near the leading-edge and the unsteady wall pressure fluctuations of the airfoil are also analyzed and the results agreed well with the experimental measurements. The present study confirms that the grid-generated approach is suitable for numerical investigation of turbulence-interaction noise and its potential mitigation strategies.

I. Nomenclature

CFD	=	Computational Fluid Dynamics	U_∞	=	free-stream velocity [m/s]
LBM	=	Lattice-Boltzmann Method	U	=	stream-wise velocity [m/s]
LES	=	Large Eddy Simulation	u	=	stream-wise velocity fluctuation [m/s]
VR	=	Variable Resolution	V	=	cross-wise velocity [m/s]
BGK	=	Bhatnagar, Gross and Krook	v	=	cross-wise velocity fluctuation [m/s]
RANS	=	Reynolds-Averaged Navier Stokes	W	=	span-wise velocity [m/s]
VLES	=	Very Large Eddy Simulation	w	=	span-wise velocity fluctuation [m/s]
FW-H	=	Ffowcs Williams-Hawkings	σ	=	grid solidity ratio
PSD	=	Power Spectral Density	TI	=	turbulence intensity
SPL	=	Sound Pressure Level	Λ_x	=	integral length scale [mm]
OASPL	=	Overall Sound Pressure Level	$E(f)$	=	Energy

*PhD Candidate, Department of Aerospace Engineering
†Research Associate, Department of Aerospace Engineering
‡PhD Candidate, Department of Flow Physics and Technology
§Assistant Professor, Department of Flow Physics and Technology, AIAA Member
¶Associate Professor, Department of Flow Physics and Technology, AIAA Member
‖Assistant Professor, DIMEAS Dept., AIAA Member
**Lecturer in Aeroacoustics, Department of Aerospace Engineering, AIAA Member
††Lecturer in Aeroacoustics, Department of Aerospace Engineering, AIAA Member

Ω	=	BGK operator	f	=	frequency
g	=	generic function	M	=	grid size [mm]
t	=	time [s]	d	=	diameter [mm]
ξ	=	particle velocity in LBM model [m/s]	τ	=	relaxation time

II. Introduction

Aircraft noise has gained substantial research interest in recent years as it is one of the leading environmental concerns [1]. Effective noise control is a challenge that the aviation industry faces. Computational Fluid Dynamics (CFD) studies can, at times, be cheaper and more extensive compared to experimental tests due to model complexity and/or wind tunnel capability [2, 3]. However, it is essential to evaluate and validate the capabilities of solvers using experimental data, and a combination of the two will lead to a more accurate and comprehensive study of problems of interest. Turbulence interaction is among some of the most important noise generation mechanisms due to its relevance and diversity of engineering applications and it arises from the turbulence distortion and scattering as it impinges on the solid body [4] . There have been numerous experimental studies on turbulence-interaction noise of airfoils and bluff bodies [5–12] and their noise mitigation strategies [13–18]. To this day, the experimental production of turbulence upstream of a solid body is being achieved with grids installed within the wind-tunnel nozzle contractions [19, 20] and have been extensively used to produce turbulent inflows since the work of Simmons and Salter [21], producing a large number of aerodynamic and aeroacoustic measurements [22–26]. These data can be used to validate CFD solvers and improve the accuracy of numerical models.

The role of CFD is to provide a cheaper and more versatile alternative to wind tunnel testing with the advantage of providing a full knowledge of the acoustic and aerodynamic behavior of the turbulence interaction processes. It also allows the study of different design configurations as well as the easy visualization of flow structures, which can be prohibitively expensive or sometimes infeasible in experimental test cases. However, the numerical setup and results needs to be validated through the use of experimental results. More than often, the main focus of numerical and analytical studies of turbulence-interaction noise has been noise abatement techniques [27–34]. These studies have improved our understanding of turbulence interaction and have further identified both turbulence intensity and the turbulence integral length scale as key parameters to accurately capture the turbulence-interaction process. There are several approaches to generate turbulence numerically, such as synthetic turbulence generation, used by Kim *et al.* [35], to investigate wavy protuberances and their noise reduction mechanisms when interacting with turbulent flow. Intuitively, turbulence production using a 'physical' grid in the computational domain is an attractive approach given its similarity to the experimental conditions. Liu *et al.* [36] performed a high-order Large Eddy Simulation (LES) to examine the turbulence generated by grids. By comparing the results between their simulation and experiments from wind tunnel test, they investigated the effect grid shape and grid position have on the characteristics of the grid-generated turbulence and concluded that it could be a viable approach in turbulence generation. In fact, much of the numerical studies investigated the production of grid-generated turbulence and their development and decay in the downstream flow [37–42]. However, there is a lack of studies conducted which utilizes the grid-generated turbulence approach to examine the turbulence interaction with aerodynamic bodies immersed in the flow. More recently, Wu *et al.* [43] reported one of the first successful attempts to investigated rotor-turbulence ingestion and noise generation from grid-generated turbulence using a solid grid setup.

The aim of this study is thus two folds: firstly to numerically investigate the development of grid-generated turbulence with a grid comparable to an actual physical set-up and hence understanding the viability of using the approach for studying turbulence interaction noise; secondly to understand and validate the flow and acoustic characteristics for turbulence interaction with a NACA0012 airfoil. The high-fidelity simulations will be carried out using a LBM solver PowerFLOW 2021 R2 and the results will be directly compared and validated with wind tunnel measurements. PowerFLOW solver has demonstrated high efficiency and scalability when it comes to large-scale numerical simulations [44–47]. Another advantage of the method is the naturally low dissipation of LBM, maintaining the resolution of turbulence convection and decay, as well as accurate capture of acoustic wave propagation due to the low point number requirement per wavelength [48]. The extensive studies conducted by Bowen *et al.* [19] will be used to validate the PowerFLOW simulations as well as provide the foundations for further numerical studies. Due to the nature of the open-jet aeroacoustic facility, several considerations must be made in order to avoid noise contamination whilst producing appropriate levels of turbulence, which have been identified and addressed by Bowen *et al.* [26]. In this work, turbulence is generated by means of a grid as their physical dimensions and turbulence generation properties in the experimental set-up are known, and hence the simulation will be a more faithful representation of the experimental

set-up. Subsequently, by directly comparing the numerical and experimental results, the grid-generated turbulence approach applied to the turbulence-airfoil interaction case can be thoroughly evaluated.

The remainder of this paper is organized as follows: A brief introduction to the Lattice Boltzmann Method and PowerFLOW is followed by the section on grid-generated turbulence, which includes the computational setup in comparison with the experimental setup and illustrations of the geometry in the simulation domain. The result comparison for turbulence intensity and integral length scale outlines the major differences between the cases and allows for modifications in order to match experimental results. A final evaluation of near-field and far field noise spectra will confirm the validity of the solver and the grid-generated turbulence implementation.

III. Lattice-Boltzmann Method

The numerical simulations were carried out using PowerFLOW, a solver based on Lattice Boltzmann Method. It uses an extended Lattice-Boltzmann model to discretize particles in space, moving in specified directions with discrete speeds and in discrete time intervals [49]. The building blocks of the simulations are cubic lattices, each 3D element is defined as a voxel, and a grid discretization scheme, which equally refines the mesh in all dimensions, scaling by a factor of two between adjacent resolution regions, also called Variable Resolution (VR) regions [50]. Within discrete timesteps, particles move from one voxel to the neighboring one. Solid objects are characterized by surfels, described as surface elements inserted where the solid intersects the fluid. The governing equation for the solver is based on the Boltzmann Equation for a gas:

$$\frac{\partial g}{\partial t} + \vec{\xi}\,\frac{\partial g}{\partial \vec{x}} + \vec{F}\,\frac{\partial g}{\partial \vec{\xi}} = \Omega, \tag{1}$$

where $g(\vec{\xi}, \vec{x}\,.t)$ represents the density of particles at time t, point x having velocity ξ [51]. The Collision Operator, Ω, is modeled by the Bhatnagar, Gross, and Krook (BGK) operator [52]:

$$\Omega = \frac{g^{(eq)} - g}{\tau}. \tag{2}$$

Here, Ω dictates that the particles after a collision will return to equilibrium within their relaxation time τ. A set of 19 discrete velocities and points in space is replaced in order to discretize the operator. This results in efficient numerical computations.

The macroscopic Boltzmann equation can be derived by integrating Eq. 1 over the microscopic velocities ξ to obtain

$$\int_{-\infty}^{\infty} \left(\frac{\partial g}{\partial t} + \vec{\xi}\,\frac{\partial g}{\partial \vec{x}} - \Omega \right) d\xi = 0. \tag{3}$$

Introducing the density and momentum equations leads to the conservation equation while multiplying the Boltzmann equation by the collision invariant ξ and performing further integration will result in the momentum conservation equations. Using ξ^2 will result in the energy equation instead [51]. The Navier-Stokes equations can be derived from LMB using the Chapman-Enskog equations [53–55].

Boundary conditions in LBM cannot be imposed by using macroscopic quantities. Therefore, the flux of particles is used instead. The two methods by which PowerFLOW determines solid boundary conditions are through the implementation of Specular Reflection or Bounce Back Reflection. In the case of the former, a net flux of particles in the x-direction and a no-net flux in the y-direction imply a u-velocity and $v = 0$ at the wall, resulting in a free-slip boundary condition. On the other hand, if particles are forced to bounce back, there is no net flux of particles in both x- and y-directions, implying that $u = 0$ and $v = 0$, leading to a no-slip boundary condition. Readers are advised to refer to existing studies for more details of the solver as well as a wide range of flow scenarios that it has been successfully used to study [29, 45, 56, 57].

IV. Turbulence-Interaction Setup

A. Experimental Setup and Grid-Generated Turbulence

Turbulence generation is the first step in understanding turbulence interaction noise propagation. In this section, both the experimental and the numerical set-up are described for the grid generated turbulence and its interaction with the airfoil downstream. The wind tunnel in which experimental results are acquired is shown in Figs. 1 and 2. The

different tested grids allowed investigation of the effect of grid spacing and sizing as well as grid position (see Fig. 1) and of the turbulence characteristics developed downstream of the grids. The results were collected for three different locations within the contraction nozzle, each having four different grids. This study will focus on the grids of the '*C*' family as denoted in [19], as it is not prohibitively large for the numerical domain.

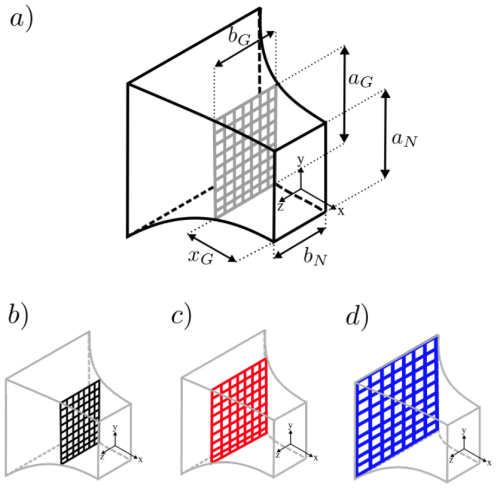

Fig. 1 Schematic of the contraction nozzle with the turbulence grids where a) is the contraction nozzle and the defining geometry definitions, b) the grid location A with a contraction ratio of 1.3, c) the grid location B with a contraction ratio of 2.4, and d) the grid location C with a contraction ratio of 4.4. Figure from Bowen *et al.* [26]

As demonstrated by Bowen *et al.* [26], the passive grids generate a turbulent wake which gradually grows into homogeneous turbulence. As the geometry imported into PowerFLOW matches the dimensions of the experimental grid and setup, the results are expected to be comparable at some downstream distance away from the grid. The advantage of using a grid to passively generate turbulence is that the turbulence develops naturally and there are no assumptions about its structure. The natural advantage that PowerFLOW offers when it comes to voxel generation (*i.e.*, meshing) of the grid, as it utilizes an efficient Cartesian mesh, which perfectly fits the geometry. The key difference between the experimental setup and the numerical simulation is the lack of the wind-tunnel nozzle and the respective contraction ratio, which comes with each of the three different locations for the grid placement, as outlined in Fig. 1. This family of grids was selected due to the abundance of data collected as well as experimentally having the lowest level of grid self-noise, resulting in accurate far field acoustics for the turbulence airfoil interaction later. Despite having the same general trend, the turbulent dissipation is predicted to be higher than that in the experimental results, which can be improved with finer meshes, as demonstrated by Blackmore *et al.* [58].

Table 1 Geometric properties, turbulence intensity and integral length scales estimated from experimental results by Bowen *et al.* [19] at the position of the contraction nozzle exit ($x = 0$), for a free-stream velocity $U_\infty = 20\,\mathrm{m\,s^{-1}}$.

Grid	Diameter, d (mm)	Mesh, M (mm)	σ	Turbulence intensity (%)	Integral length scale (mm)
C-2	19	100	0.35	4.9	6.1

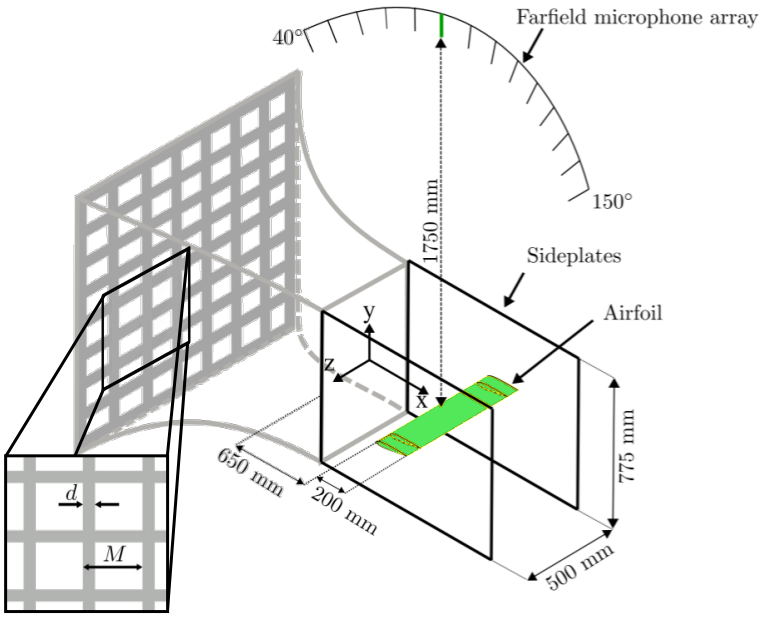

Fig. 2 Schematics of the contraction nozzle with a representative turbulence grid and the setup of the NACA0012 airfoil and geometric definition of the grids from Bowen *et al.* [19]

B. Computational Setup

The simulation setup is based on the works of Bowen *et al.* [19] in Fig. 2, who conducted extensive tests on different grid configurations as well as angles of attack of a NACA0012 airfoil placed in the wake of the grid. The chosen grid out of the four available configurations is grid '*C2*' [26], with geometric and turbulent properties outlined in Table 1. The simulation domain can be seen in Fig. 3.

Experimental tests have demonstrated that generated turbulent scales are proportional to the grid size (M) and decay downstream [58], hence, a sufficiently large domain must be set up to allow both sufficient development length of the turbulence as well as to minimize potential interference of the generated turbulence from the boundary conditions. The simulation domain of the present numerical set-up is $8.8\,\mathrm{m} \times 4.8\,\mathrm{m} \times 0.4\,\mathrm{m}$, which was sized based on the mesh size (M) to allow for a total of 4 grid holes in the span-wise direction, with periodic boundary conditions in the y- and z-direction so that the geometry of the contraction nozzle does not need to be modeled. This can therefore be considered as a straight enclosed wind tunnel with the grid filling the tunnel dimensions. As there are no losses in the y- and z-direction and the only outlet is placed downstream, the velocity is expected to recover to free-stream as suggested by the previous study [36]. As the simulation domain is sufficiently large with adequate voxel coarsening and periodic boundary conditions, acoustic wave reflection at the far field boundaries were not observed and thus are of no particular concern.

The inlet velocity is set to $20\,\mathrm{m\,s^{-1}}$ to recover the same free-stream velocity as in the experiments, which corresponds to a chord-based Reynolds number of $Re = 2.7 \times 10^5$. The outlet is defined as a pressure outlet at 101 325 Pa, standard atmospheric condition. The finest VR region to maintain low numerical dissipation of turbulence extends from the grid to three chords downstream of the leading edge in x-direction (*i.e.*, stream-wise). This gives the size of the voxel in this VR region as 7.81×10^{-4} m, which is small enough to encourage appropriate evolution and convection of the generated turbulence downstream. Additional VR regions are added around the airfoil to reduce the smallest voxel size down to 9.77×10^{-5} m in order to accurately resolve the boundary layer and the range of turbulence length scales arising from interaction with the airfoil, giving the total voxel count for the simulation to approximately 1236 million.

For computing the far field acoustics, the present simulation utilizes the solid formulation of the Ffowcs Williams-Hawkings (FW-H). The noise acquisition frequency is set to 20 kHz to ensure the desirable range of frequencies is captured based on Nyquist criterion. To examine the evolution of the velocity fields, a x-z measurement plane at $y = 0$ was also recorded at identical sampling frequency. Prior to data collection, a velocity analysis helped determine a transient time of around 20 flow passes, which then allowed the value of total simulation duration to be refined.

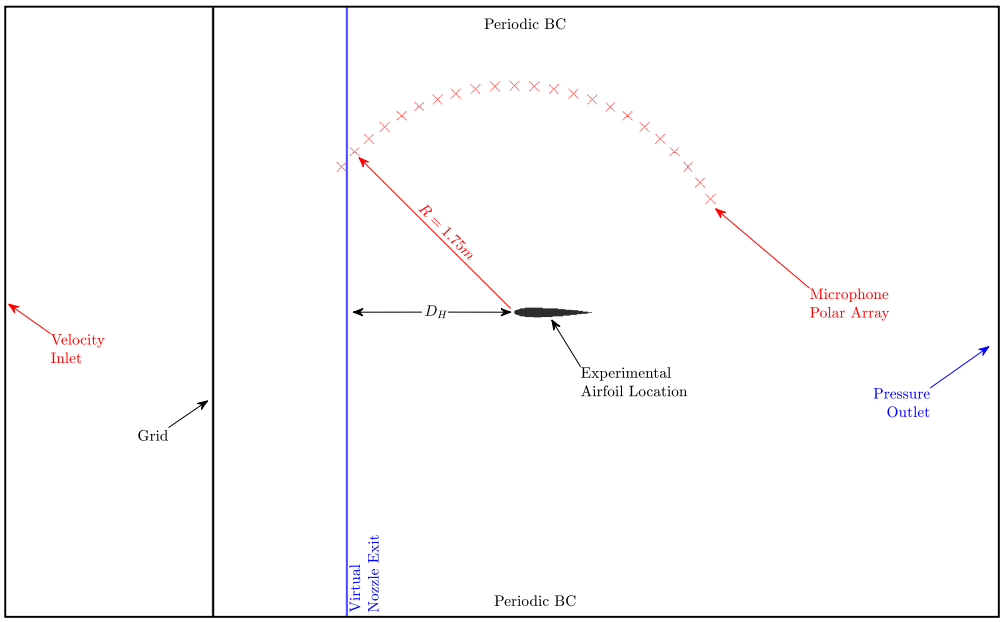

Fig. 3

Fig. 4 Simulation setup for grid-generated turbulence, including the locations of the experimental nozzle exit and airfoil (boundaries and airfoil not to scale).

V. Results

A. Turbulent Characteristics

In order to understand the flow and turbulence characteristics and assess whether the solver has the capability of accurately resolving the turbulence generated by the grid and its development, simulations with the grid alone (*i.e.*, no airfoil in the domain) was carried out. Results from Bowen *et al.* [19] have been compared to numerical results at the same locations and under the same parameters. Experimental results have been collected from the nozzle exit and up to $1.5x/D_H$ downstream, where $D_H = 0.65$ m is the hydraulic diameter of the wind-tunnel nozzle exit. On the other hand, the velocity field statistics are registered at the exit of the grid to several D_H downstream, permitting the analysis of the turbulence generation and evolution at all of the stages. Turbulence intensity and integral length scale are calculated as a function of downstream distance in x-direction. The turbulence intensity, *TI*, can be calculated as:

$$TI = \frac{1}{U_\infty}\sqrt{\frac{1}{3}(u'^2 + v'^2 + w'^2)}, \tag{4}$$

where u', v', and w' are the turbulent velocity fluctuations in the stream-, cross- and span-wise directions, respectively. Fig. 5 illustrates the turbulence intensity as a function of x/D_H along the mid-span of the simulation domain. The location of the 'Experimental Nozzle Exit' is denoted by the solid vertical line, while the 'Experimental Airfoil' is located at $x/D_H = 1$, which coincides with the Virtual Nozzle Exit location, and hence indicated in Fig. 5. These match the x/D_H location displayed in Fig. 2. As can be seen from the comparison, in order to match well with the experimental nozzle exit vale of turbulence intensity of 4.9%, the so-called 'nozzle-exit' location from the numerical simulation appears further downstream from the original location of $x/D_H = 0$, and it is moved to $x/D_H = 1$, in reference to the experimental set-up in [19]. This is labeled in Fig. 5 as the 'Virtual Nozzle Exit'. It can be observed that the turbulence intensity decay trend of the numerical simulation matched well with the experiments beginning at the nozzle exit to $x/D_H = 1$ downstream (presumably when the two exits are aligned, as seen in Fig. 5. Consequently, the location of the airfoil in the numerical set-up has also been shifted downstream to maintain the original 650 mm distance (one hydraulic diameter, D_H) from the nozzle exit, having consistent trend with the experiments. Note that the location of the airfoil in the numerical set-up is denoted by the green dashed line, labeled 'Virtual Airfoil'.

Grid-generated turbulence is empirically known to become isotropic at 20 mesh-sizes downstream of the grid [38],

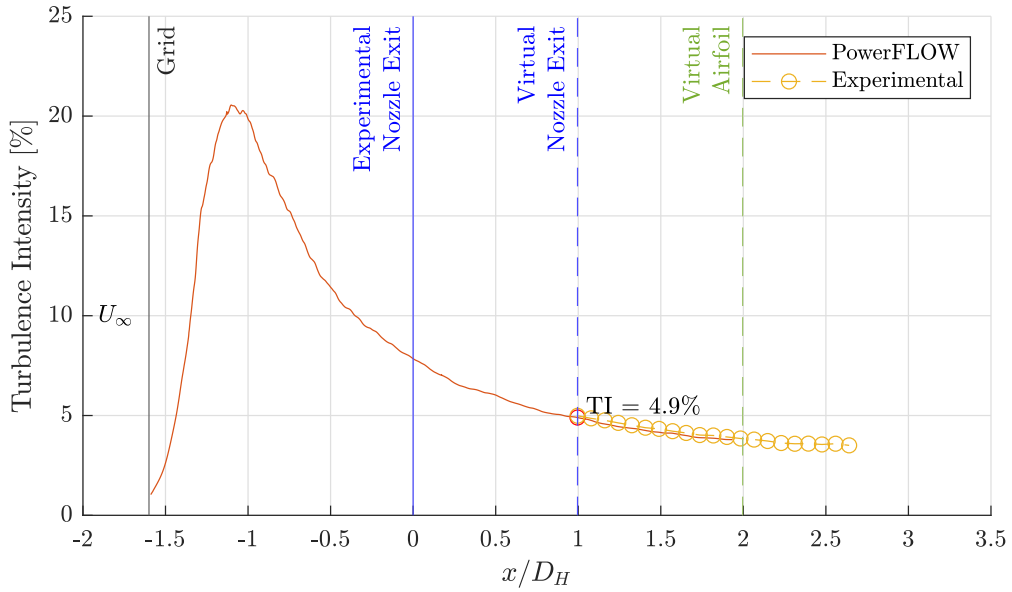

Fig. 5 Numerical and experimental results for turbulence intensity of the *C2* grid.

which in the case of the current grid, equates to a downstream distance of 2000 mm which is equivalent to $1.48x/D_h$ downstream of the location of the nozzle exit. However, as shown by Comte-Bellot and Corrsin [22], the absence of the contraction nozzle from the numerical grid set-up delays the decay as well as the downstream location at which the isotropy and homogeneity of the generated turbulence become comparable to the experimental measurements. Therefore, it is equally important to validate the integral length scales and the anisotropy level of the turbulence against the experiments at the corresponding downstream locations. Firstly, the integral length scale is calculated based on [24, 59], which has been widely used:

$$\Lambda_x = \left[\frac{E(f)U_{mean}}{4\bar{u}^2} \right]_{f\to 0}, \tag{5}$$

where $\bar{u}$ is the standard deviation of the U velocity. The magnitude of the energy spectra $E(f)$ as frequency f approaches zero is evaluated by averaging the first 80 points, where the values of these points at low frequencies asymptotically converge. The integral length scale was calculated this way both as a function of x as well as in the span-wise direction for the location of the 'Virtual Nozzle Exit' at $x/D_H = 1$. As outlined by Blackmore *et al.* [58], the integral length is highly mesh-dependent and stabilizes for higher-resolution meshes. Therefore, a grid dependence study has also been conducted on a smaller simulation domains to assess the impact resolution has on integral length scale. It was determined that the chosen resolution for the simulation presented is considered stable and grid-converged. It can be seen from Fig. 6 that the trend of the length scale matches well with the experimental measurements up to the location of the airfoil. At the 'Virtual Nozzle Exit' location, the length scale evaluated from the simulation is 6.0 mm, which is comparable to the experimental result of 6.1 mm. Moreover, the span-wise averaged length scale, denoted by the larger red cross symbol in Fig. 6, also agrees well with that determined at the center location, suggesting that the turbulence generation is uniform in the span-wise direction and current periodic boundary condition are suitable for the turbulence generation process. The subsequent increase of Λ_x observed from the experiments is possibly attributed to the dissipative nature of the open-jet configuration. However, since the turbulence interaction with the airfoil mainly concerns the inflow conditions, *i.e.* the turbulence characteristics impinging upon the leading-edge of the airfoil, the present agreement is deemed satisfactory for the turbulence-airfoil interaction simulations.

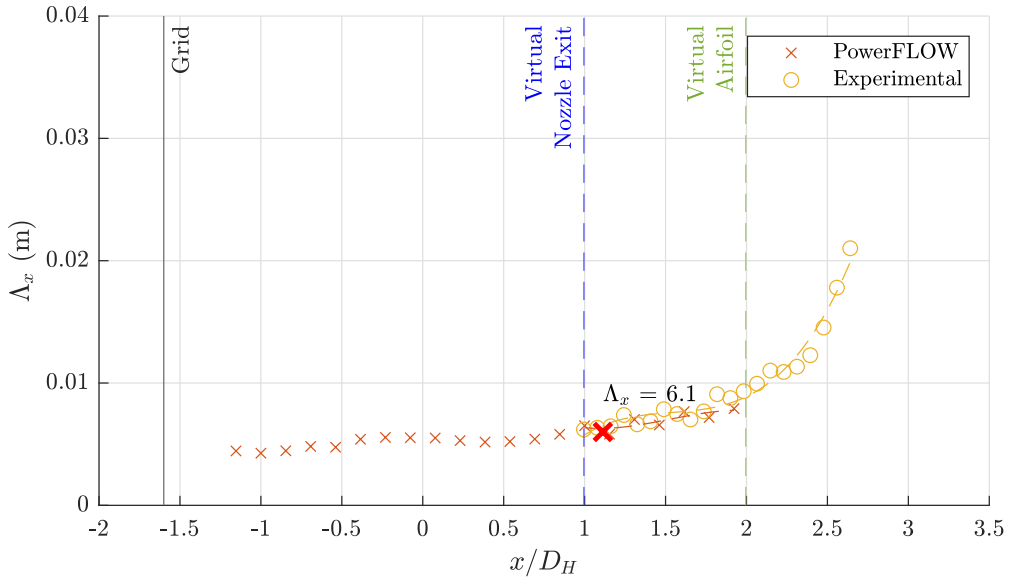

Fig. 6 Numerical and experimental results for integral length scale of the *C2* grid.

A blown-up, finalized version of the grid-airfoil setup can be seen in Fig. 7.

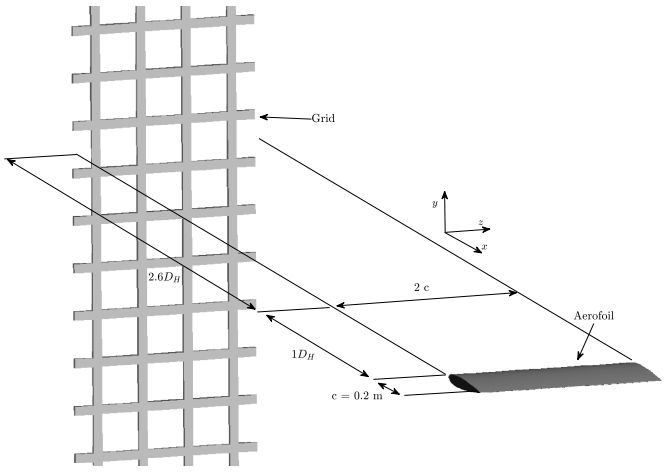

Fig. 7 Schematic of the grid-airfoil setup and coordinate system.

Secondly, by extracting the values of the root-mean-square (r.m.s.) velocity fluctuations, the anisotropy levels of the turbulence at airfoil location can be computed as:

$$\beta_{uv} = 1 - \frac{u'}{v'}, \quad \beta_{uw} = 1 - \frac{u'}{w'}. \tag{6}$$

The results from Eq. 6 confirm the isotropy of the turbulence as the values of $\beta_{uv} \approx \beta_{uw} \approx 0$ since $u' \approx v' \approx w'$. This is in slight contrast with the experimental results from Bowen *et. al* [19], since the turbulence generated in the experiments still exhibit some extent of anisotropy upstream of the leading-edge of the airfoil. This can possibly be explained by the use of periodic boundary conditions and the lack of the contraction nozzle in the simulation. The effect of the differences between isotropic and anisotropic turbulence has not been experimentally and numerically investigated, and could be of interest for prospective studies. Lastly, Fig. 8 shows the contours of vorticity magnitude,

which provides a good indication of the development of the flow. It can be seen that downstream of the grid, the turbulence can be considered homogeneous in both the $y-$ and $z-$directions, having little difference in either direction. The grid location is represented by the vertical white line and the location of the Virtual Nozzle Exit is now located at $x/D_H = 0$. Comte-Bellot *et al.* [22] concluded that the use of a contraction nozzle produces a turbulence field which appears to be more homogeneous and isotropic than reported by previous studies [60] and can be considered statistically homogeneous and isotropic by 20 mesh lengths downstream of the grid [38]. The vorticity fluctuations are computed at this location and they were found to be within 500 $1/s$ in both the z- and y-direction. Further simulations also confirm that the alignment of the grid has no effect on the downstream turbulence statistics relevant to this study and, therefore, the chosen span is sufficient to simulate the desired turbulence interaction in the span-wise and cross-stream directions.

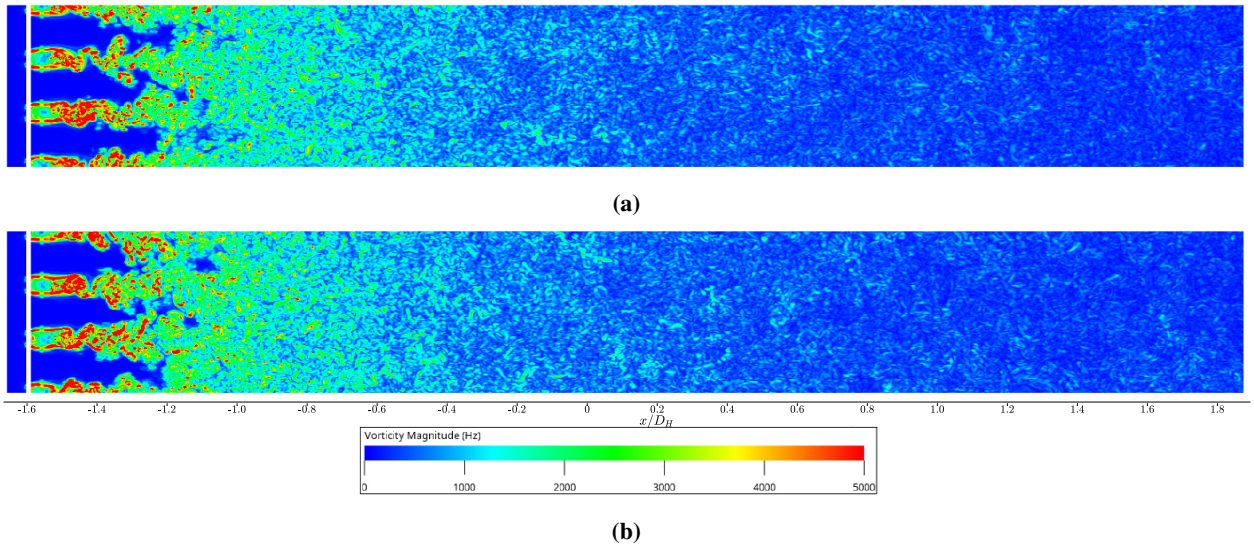

Fig. 8 Vorticity magnitude in the (a) span-wise (y-aligned) plane and (b) cross-wise (z-aligned) plane.

B. Turbulence interaction with the NACA 0012 airfoil

After the initial grid-only simulations to extract the turbulence intensity, integral length scale, and anisotropy to assess the feasibility of a comparison between experimental and numerical setups, the airfoil is placed at the location downstream of the grid that matches the required length scale and intensity. Subsequently, the main aerodynamic characteristics such as the velocity and velocity fluctuation decay, static and unsteady surface pressure as well as the far field acoustics were recorded and compared to the experimental measurement wherever possible. First of all, non-dimensional time-averaged pressure coefficient (C_p) along the surface of the airfoil is presented in Fig. 9 (a). The pressure coefficient distribution obtained from the viscous formulation of XFoil at similar Reynolds and Mach numbers to the numerical simulation is also overlaid. Since XFoil cannot model the turbulence levels achieved in the PowerFLOW case, the airfoil is 'manually' tripped close to the leading edge, allowing for the turbulent boundary layer to develop immediately, which replicates the effect the incoming turbulent flow has on the airfoil's leading edge. As seen in Fig. 9(a), a close match of the simulation and XFoil results reaffirms that the present simulation is able to correctly predict the mean aerodynamic behavior of the turbulence-airfoil interaction.

Turbulence intensity and integral length scale at the airfoil leading edge are critical to the aerodynamic and aeroacoustic performance of the turbulence interaction process. Their magnitudes have been identified in the previous section to match experimental results and therefore are not evaluated again for the simulation with the airfoil. In addition, as the body creates a velocity stagnation at the leading edge, its hydrodynamic field is likely to affect the flow upstream, thus altering the decay and distortion of the turbulent structures upstream of the leading edge. As a result, in order to assess the effect of the airfoil has on the flow upstream, mean and fluctuating velocity fields are extracted along a stagnation line from $x/r = 0$, which corresponds to the location of the leading edge and where r denotes the leading edge radius $r = 3.17$ mm. Fig. 9 (b) shows the changes of the mean and fluctuating velocity components up to five leading edge radii. The left y-axis depicts the evolution of the stream-wise component of velocity, normalized by the free-stream velocity (U/U_∞), where $U_\infty = 20\,\mathrm{m/s}$. The right y-axis represents the root-mean-square (r.m.s.) of

the velocity fluctuations $\sqrt{u'^2 + v'^2}/\sqrt{u_0'^2 + v_0'^2}$, where $\sqrt{u_0'^2 + v_0'^2}$ is the free-stream r.m.s. of the velocity fluctuations extracted at $(x/r = -32)$. Experimental results are included for comparison and are depicted by the circle and triangle markers respectively. Similarly to experimental results, the velocity fluctuations are only considered in the stream- and cross-stream directions. As depicted in the figure, the overall trend of the stagnation line is followed and is consistent with experimental results from Bowen *et al.* [61]. As expected, the velocity at the stagnation point $x/r = 0$ would have zero velocity, which the simulation correctly captures. The mean stream-wise velocity approaches approximately 90% of the free-stream velocity at $x/r = 5$ upstream, similarly to the experimental results, while the recovery of the r.m.s. is considerably slower than the free-stream r.m.s. of velocity fluctuations, which implies a larger effect on the flow from the presence of the leading edge stagnation. It is important to note that due to the availability of the experimental data, the location of the airfoil for the experimental results presented in 9 (b) is $x = 350$ mm downstream of the nozzle rather than the $x = 650$ mm of the previously discussed experimental results by Bowen *et al.* [19]. Furthermore, the turbulence was produced by the C1 grid (refer to Appendix A). Despite it having similar turbulence-generation characteristics, the C1 grid differs from the C2 grid used in the simulation and in the previous comparisons, therefore, some discrepancies are expected in the fluctuating components between the simulation and the experiments. Yet, as will be seen in the following section, the resulting near-field surface pressure fluctuation spectra and far field noise spectra agree well between the two, despite the differences in the recovery of the velocity fluctuations.

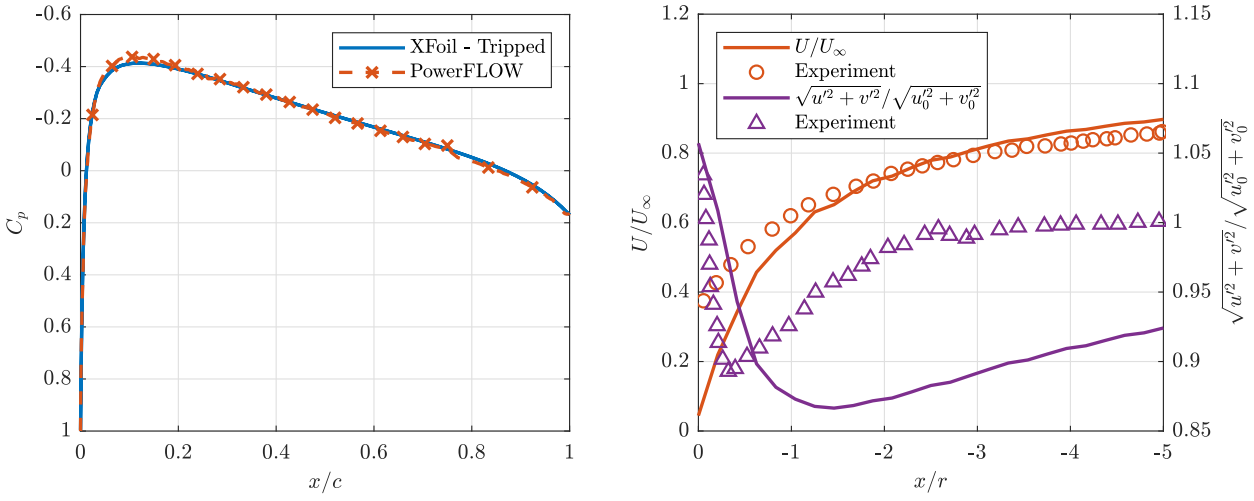

Fig. 9 Comparison of (a) Mean pressure coefficient C_p for the NACA0012 airfoil from XFoil and PowerFLOW and (b) Stagnation line evolution of the stream-wise component of velocity U/U_∞ (left axis) and root-mean-square of the velocity fluctuations $\sqrt{u'^2 + v'^2}/\sqrt{u_0'^2 + v_0'^2}$ (right axis) from PowerFLOW (solid lines) and experiment (markers)

C. Near- and far field aeroacoustic characteristics

The flow solution from PowerFLOW is inherently unsteady and compressible, and the low dissipation and dispersion make it suitable for aeroacoustic measurements by extracting pressure fluctuations on the surface or in the near field [62]. Differently from the experiment, the far field noise analysis from direct measurements is unattainable with the current simulation volume setup. The microphone polar array from Bowen *et al.* [19] are placed at 1.75 m radially out from the leading edge (90°), arranged in increments of 5° between the angles of 40° and 150°, which is considered to be in the far field in the anechoic chamber. The same polar array is recreated in PowerFLOW using pressure measurements from the surface of the airfoil and subsequently integrated and propagated with the FW-H analogy to obtain the far field acoustics [63, 64]. The FW-H implementation and post-processing of the noise spectra have already been used and validated in a number of studies [56, 62, 64, 65], which demonstrated good comparison and robustness. As previously mentioned, the solid FW-H surface is sampled at 20 kHz to ensure sufficient sampling rate for comparison

with experimental acoustic spectra. The Power Spectral Density (PSD), expressed in dB/Hz, is calculated as

$$\mathrm{PSD} = 10\log_{10}(\phi_{pp}/p_0^2), \tag{7}$$

where ϕ_{pp} is the pressure fluctuation power in the frequency domain evaluated by the Welch's estimate function and $p_0 = 20\,\mu$Pa is the reference pressure. The present study only takes into account the far field noise results of the turbulence interaction with the NACA0012 airfoil as it would be prohibitively expensive to record solid FW-H data from the surface of the grid itself. Furthermore, as outlined by Bowen *et al.* [19], the grids at location C have a self-noise level within 3 dB/Hz of the background levels.

Using the FW-H analogy, it was possible to produce the far field noise comparisons for the spectra from individual microphone at the polar angle of 90°, as shown in Fig. 10(a) as well as for overall sound pressure level (OASPL) directivity computed from all of the microphones along the array, as shown in Fig. 10(b). The background grid self-noise from the experiment is included for reference. Clearly, the numerical simulation predicts the increase of the far field noise in the low-to-medium frequency range from approximately 200Hz to 1000Hz, as manifested by the broadband hump above the background noise. An additional hump from approximately 1000Hz to 1600Hz can be observed from the simulation, different from that of the experimental results, which requires further investigation. It is worthwhile mentioning that similar broadband humps at approximately 1000Hz were seen in the experimental results of other passive grids. At even higher frequencies, the magnitudes of the PSD spectra begin to differ from experimental values. However, it is likely that the experimental measurements were influenced by the background noise at higher frequencies. Yet, the gradient of the decay remains comparable. Nonetheless, the overall performance of the far field noise prediction from the present grid-generated turbulence interacting with the airfoil is considered satisfactory. The directivity of the overall sound pressure levels shown in Fig. 10 (b) further corroborates the notion as good agreements can be observed between the two for the OASPL directivity. In fact, the differences of the OASPL computed from the present simulation is within 4 dB of the experimental measurements. Lockard [66] performed a study comparing the solid and permeable FW-H formulation in PowerFLOW and demonstrated that there exists some differences in capturing the far field noise spectra from the two formulations, and hence could be of interest in the prospective study.

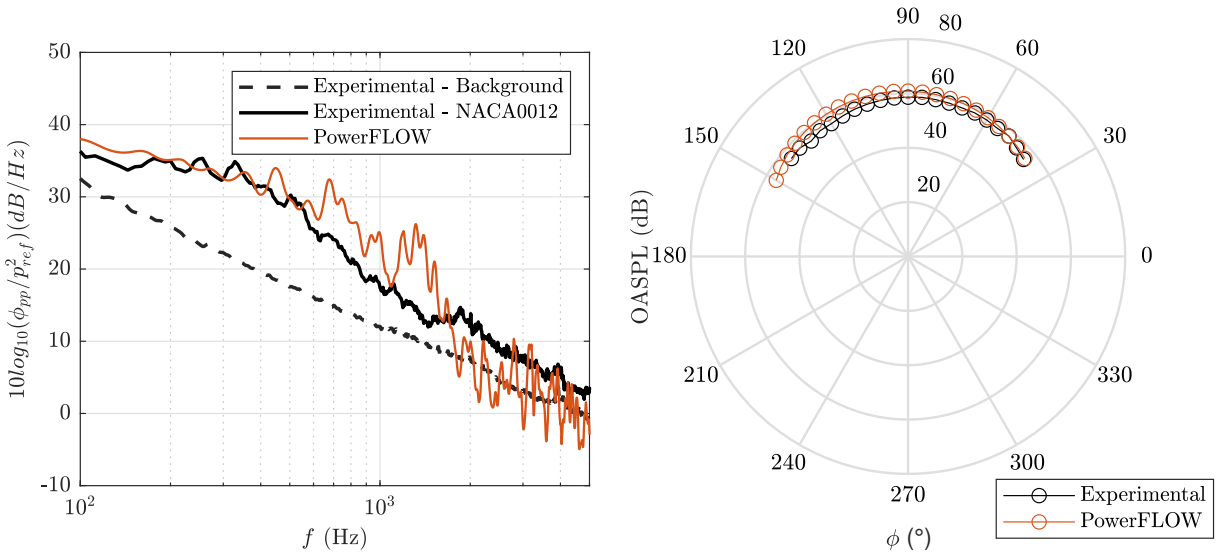

(a) **(b)**

Fig. 10 Far field (a) Noise sound pressure level comparison between experimental data and solid FW-H from PowerFLOW simulation measured at $\theta = 90°$ and (b) Overall sound pressure level directivity comparison between experimental data and solid FW-H from PowerFLOW simulation

In addition to the far field acoustics, the near-field aeroacoustic characteristics in the form of surface pressure fluctuation spectra is obtained and compared with the experiments, which ensures consistency between the near-field and far field prediction from the present simulation study. As shown by Bowen *et al.* [61], the surface pressure fluctuation spectra experience a significant increase in locations closer to the airfoil leading edge due to the inflow turbulence.

Therefore, the surface pressure fluctuations at two airfoil locations close to the leading edge at $x/c = 0$ (p1) and $x/c = 0.08$ (p2) were extracted, similar to the experiments. it should again be remarked that these results were taken from the 'C1' grid, but they reflect well the general behavior of the surface pressure fluctuation spectra for turbulence interaction with the airfoil.

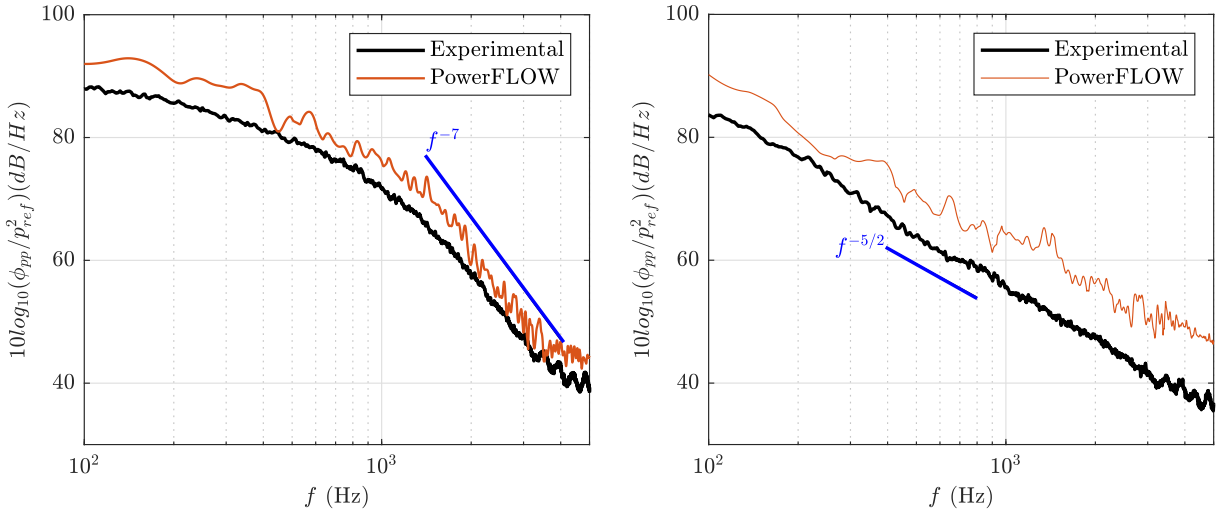

Fig. 11 Power Spectral Density of the surface pressure fluctuations comparison between experimental and numerical results over the NACA0012 airfoil for (a) transducer p1 located at the leading edge and (b) transducer p2 located at $x/c = 0.08$.

As expected, the highest surface pressure fluctuation energy level is generated at the stagnation point and a close match is observed between numerical and experimental results, which is presented in Fig. 11(a). The surface pressure fluctuation spectra scale with f^{-7} at high frequencies, similar to experimental data, however the low-frequency energy level has a magnitude higher by an almost consistent 4 dB/Hz. Consistent results are also obtained after the stagnation point for probe p2, for which the surface pressure fluctuation spectra scale with $f^{-5/2}$ as shown in Fig. 11(b). The magnitude of the spectra is however higher by an approximately constant 7 dB/Hz, which could possibly be attributed to the difference in the grids used. The increase observed in the near-field surface pressure fluctuations correspond well with those increase in the far field noise across the frequency range of interest, and possibly contributes to the increase, as calculated from the FW-H analogy. The results from the far field noise spectra suggest that the leading edge region of the airfoil is the biggest contributor to the airfoil-turbulence interaction noise.

VI. Conclusion

Grid-generated turbulence using square grids is a complicated mechanism that requires small adjustments in order to numerically replicate the experimental results. Turbulence interaction noise computed using the FW-H solid analogy is used to compare to experimental far field measurements. The results from this study suggest that the simulation of leading edge grid-generated turbulence interaction using the LBM solver PowerFLOW can produce comparable results to the experimental setup by Bowen *et al.* [19]. Due to the lack of certain flow and surface measurements from experimental results involving the C2 grid, some comparative studies were conducted using a grid that produces similar turbulent characteristics and has overall more consistent results for the variables of interest. However, the location of the airfoil in the setup with this grid differs from the location used both in the experimental and numerical setups. PowerFLOW has been successfully used for simulations involving far field noise computations; therefore, the authors are confident that adjusting the location of the airfoil will produce results that will be more consistent with the experimental results of Bowen *et al.* [61]. Despite this difference, both turbulence characteristics, far field noise computations, and surface pressure SPL have compared well to experimental data, with only minor differences. Some of the problems observed herein, such as the discrepancies in high-frequency noise spectra, OASPL, and surface pressure SPL for the probe locations further along the airfoil chord, are likely to be due to grid-self noise, which is better damped out in

experimental results. In addition, the use of solid acoustic data for the FW-H analogy could prove insufficient, and therefore a comparison using permeable surface acoustic data should be considered. New simulations will be set up to explore the new location of the airfoil downstream of the grid in order to better compare with experimental data and understand if there are any incorrect assumptions being made when setting up the simulation and in the use of the FW-H analogy, which leads to higher energy spectra values as shown in this study. The implementation of the correct acoustic analogy will allow for the exploration of different angles of attack and leading edge variations to efficiently investigate the noise spectra and subsequently noise-abatement techniques.

VII. Acknowledgements

The authors would like to acknowledge the EPSRC DTP programme with grant number 1708912 for the PhD scholarship.

References

[1] Nagy, A. B., Delfs, J., and Bennett, G. J., "Aeroacoustics research in Europe: The CEAS-ASC report on 2020 & 2021 highlights," *Journal of Sound and Vibration*, Vol. 534, 2022, p. 117002. https://doi.org/10.1016/j.jsv.2022.117002.

[2] Slotnick, J., Khodadoust, A., Alonso, J., and Darmofal, D., "CFD Vision 2030 Study: A Path to Revolutionary Computational Aerosciences," *NNASA/CR-2014-218178*, 2014. URL http://www.sti.nasa.gov.

[3] Udoewa, V., Kumar, V., Udoewa, V., and Kumar, V., "Computational Fluid Dynamics," *Applied Computational Fluid Dynamics*, 2012. https://doi.org/10.5772/28614, URL https://www.intechopen.com/state.item.idundefined/state.item.id.

[4] Amiet, R. K., "Acoustic radiation from an airfoil in a turbulent stream," *Journal of Sound and Vibration*, Vol. 41, No. 4, 1975, pp. 407–420. https://doi.org/10.1016/S0022-460X(75)80105-2.

[5] Mish, P. F., and Devenport, W. J., "An experimental investigation of unsteady surface pressure on an airfoil in turbulence-Part 2: Sources and prediction of mean loading effects," *Journal of Sound and Vibration*, Vol. 296, No. 3, 2006, pp. 447–460. https://doi.org/10.1016/j.jsv.2005.08.009.

[6] Mish, P. F., and Devenport, W. J., "An experimental investigation of unsteady surface pressure on an airfoil in turbulence-Part 1: Effects of mean loading," *Journal of Sound and Vibration*, Vol. 296, No. 3, 2006, pp. 417–446. https://doi.org/10.1016/j.jsv.2005.08.008.

[7] Geyer, T. F., Lucius, A., Schrödter, M., Schneider, M., and Sarradj, E., "Reduction of turbulence interaction noise through airfoils with perforated leading edges," *Acta Acustica united with Acustica*, Vol. 105, No. 1, 2019, pp. 109–122. https://doi.org/10.3813/AAA.919292.

[8] Bowen, L., Celik, A., Azarpeyvand, M., and da Silva, C. R., "Porous geometry effects on the generation of turbulence interaction noise," *AIAA Aviation and Aeronautics Forum and Exposition, AIAA AVIATION Forum 2021*, American Institute of Aeronautics and Astronautics Inc, AIAA, 2021. https://doi.org/10.2514/6.2021-2193, URL https://arc.aiaa.org/doi/10.2514/6.2021-2193.

[9] Bowen, L., Celik, A., Azarpeyvand, M., and Westin, M. F., "The effect of angle of attack on turbulence interaction noise with a porous leading edge," *28th AIAA/CEAS Aeroacoustics Conference, 2022*, American Institute of Aeronautics and Astronautics Inc, AIAA, 2022. https://doi.org/10.2514/6.2022-3095, URL https://arc.aiaa.org/doi/10.2514/6.2022-3095.

[10] Chaitanya, P., Narayanan, S., Joseph, P., Vanderwel, C., Turner, J., Kim, J. W., and Ganapathisubramani, B., "Broadband noise reduction through leading edge serrations on realistic aerofoils," *21st AIAA/CEAS Aeroacoustics Conference*, 2016. https://doi.org/10.2514/6.2015-2202, URL http://arc.aiaa.org.

[11] Kurian, T., and Fransson, J. H., "Grid-generated turbulence revisited," *Fluid Dynamics Research*, Vol. 41, No. 2, 2009, p. 021403. https://doi.org/10.1088/0169-5983/41/2/021403, URL https://iopscience.iop.org/article/10.1088/0169-5983/41/2/021403https://iopscience.iop.org/article/10.1088/0169-5983/41/2/021403/meta.

[12] Geyer, T. F., Sarradj, E., and Hobracht, M., "Noise generated by a leading edge in anisotropic turbulence," *Proceedings of the INTER-NOISE 2016 - 45th International Congress and Exposition on Noise Control Engineering: Towards a Quieter Future*, 2016, pp. 6067–6078. URL https://www.researchgate.net/publication/307569874_Noise_generated_by_a_leading_edge_in_anisotropic_turbulence.

[13] Geyer, T. F., and Sarradj, E., "Self Noise Reduction and Aerodynamics of Airfoils With Porous Trailing Edges," *Acoustics*, Vol. 1, No. 2, 2019, pp. 393–409. https://doi.org/10.3390/acoustics1020022, URL https://www.mdpi.com/2624-599X/1/2/22/htmhttps://www.mdpi.com/2624-599X/1/2/22.

[14] Roger, M., Schram, C., and de Santana, L., "Reduction of airfoil turbulence-impingement noise by means of leading-edge serrations and/or porous materials," *19th AIAA/CEAS Aeroacoustics Conference*, 2013, p. 105. https://doi.org/10.2514/6.2013-2108, URL https://arc.aiaa.org/doi/10.2514/6.2013-2108.

[15] Narayanan, S., Chaitanya, P., Haeri, S., Joseph, P., Kim, J. W., and Polacsek, C., "Airfoil noise reductions through leading edge serrations," *Physics of Fluids*, Vol. 27, No. 2, 2015, p. 025109. https://doi.org/10.1063/1.4907798, URL https://aip.scitation.org/doi/abs/10.1063/1.4907798.

[16] Celik, A., Mayer, Y. D., and Azarpeyvand, M., "On the aeroacoustic characterization of a robust trailing-edge serration," *Physics of Fluids*, Vol. 33, No. 7, 2021, p. 075120. https://doi.org/10.1063/5.0054767, URL https://aip.scitation.org/doi/abs/10.1063/5.0054767.

[17] Lyu, B., and Azarpeyvand, M., "On the noise prediction for serrated leading edges," *Journal of Fluid Mechanics*, Vol. 826, 2017, pp. 205–234. https://doi.org/10.1017/jfm.2017.429, URL https://www.cambridge.org/core/journals/journal-of-fluid-mechanics/article/abs/on-the-noise-prediction-for-serrated-leading-edges/085BA8075FC9A1812489A0AA16495461.

[18] Palleja-Cabre, S., Chaitanya, P., Joseph, P., Kim, J. W., Priddin, M. J., Ayton, L. J., Geyer, T. F., and Chong, T. P., "Downstream porosity for the reduction of turbulence-aerofoil interaction noise," *Journal of Sound and Vibration*, Vol. 541, 2022, p. 117324. https://doi.org/10.1016/j.jsv.2022.117324.

[19] Bowen, L., Celik, A., Azarpeyvand, M., and da Silva, C. R., "Grid Generated Turbulence for Aeroacoustic Facility," *AIAA Journal*, Vol. 60, No. 3, 2022, pp. 1833–1847. https://doi.org/10.2514/1.J060851.

[20] Paruchuri, C., "Aerofoil geometry effects on turbulence interaction noise," Ph.D. thesis, University of Southampton, 4 2017. URL https://eprints.soton.ac.uk/415884/.

[21] Simmons, L. F. G., and Salter, C., "Experimental investigation and analysis of the velocity variations in turbulent flow," *Proceedings of the Royal Society of London. Series A, Containing Papers of a Mathematical and Physical Character*, Vol. 145, No. 854, 1934, pp. 212–234. https://doi.org/10.1098/rspa.1934.0091, URL https://royalsocietypublishing.org/doi/10.1098/rspa.1934.0091.

[22] Comte-Bellot, G., and Corrsin, S., "The use of a contraction to improve the isotropy of grid-generated turbulence," *Journal of Fluid Mechanics*, Vol. 25, No. 4, 1966, pp. 657–682. https://doi.org/10.1017/S0022112066000338, URL https://www.cambridge.org/core/journals/journal-of-fluid-mechanics/article/use-of-a-contraction-to-improve-the-isotropy-of-gridgenerated-turbulence/CACE87D11E6F16B961C55AC28037DA78https://doi.org/10.1017/S0022112066000338.

[23] Uberoi, M. S., and Wallis, S., "Effect of grid geometry on turbulence decay," *Physics of Fluids*, Vol. 10, No. 6, 1967, pp. 1216–1224. https://doi.org/10.1063/1.1762265.

[24] Roach, P. E., "The generation of nearly isotropic turbulence by means of grids," *International Journal of Heat and Fluid Flow*, Vol. 8, No. 2, 1987, pp. 82–92. https://doi.org/10.1016/0142-727X(87)90001-4.

[25] Liu, R., Ting, D. S., and Rankin, G. W., "On the generation of turbulence with a perforated plate," *Experimental Thermal and Fluid Science*, Vol. 28, No. 4, 2004, pp. 307–316. https://doi.org/10.1016/S0894-1777(03)00106-7.

[26] Bowen, L., Celik, A., Azarpeyvand, M., and da Silva, C. R., "Design and analysis of turbulence grids for aeroacoustic measurements," *AIAA AVIATION 2020 FORUM*, 2020, pp. 1–12. https://doi.org/10.2514/6.2020-2525.

[27] Lau, A. S., Haeri, S., and Kim, J. W., "The effect of wavy leading edges on aerofoil-gust interaction noise," *Journal of Sound and Vibration*, Vol. 332, No. 24, 2013, pp. 6234–6253. https://doi.org/10.1016/j.jsv.2013.06.031.

[28] Gea-Aguilera, F., Gill, J., Angland, D., and Zhang, X., "Wavy leading edge airfoils interacting with anisotropic turbulence," *23rd AIAA/CEAS Aeroacoustics Conference, 2017*, 2017. https://doi.org/10.2514/6.2017-3370, URL http://arc.aiaa.org.

[29] van der Velden, W. C., and Casalino, D., "Towards digital noise certification of serrated wind turbines," *25th AIAA/CEAS Aeroacoustics Conference, 2019*, American Institute of Aeronautics and Astronautics Inc, AIAA, 2019. https://doi.org/10.2514/6.2019-2646.

[30] Teruna, C., Rego, L., Casalino, D., Ragni, D., and Avallone, F., "A Numerical Study on Aircraft Noise Mitigation Using Porous Stator Concepts," *Aerospace*, Vol. 9, No. 2, 2022. https://doi.org/10.3390/aerospace9020070.

[31] Rego, L., Avallone, F., Ragni, D., and Casalino, D., "On the mechanisms of jet-installation noise reduction with flow-permeable trailing edges," *Journal of Sound and Vibration*, Vol. 520, 2022. https://doi.org/10.1016/j.jsv.2021.116582.

[32] Jawahar, H. K., and Azarpeyvand, M., "Numerical investigation of high-lift airfoil fitted with slat cove filler," *25th AIAA/CEAS Aeroacoustics Conference, 2019*, 2019. https://doi.org/10.2514/6.2019-2439, URL http://arc.aiaa.org.

[33] Zamponi, R., Satcunanathan, S., Moreau, S., Ragni, D., Meinke, M., Schröder, W., and Schram, C., "On the role of turbulence distortion on leading-edge noise reduction by means of porosity," *Journal of Sound and Vibration*, Vol. 485, 2020, p. 115561. https://doi.org/10.1016/j.jsv.2020.115561.

[34] Zamponi, R., Satcunanathan, S., Moreau, S., Meinke, M., Schröder, W., and Schram, C., "Effect of porosity on Curle's dipolar sources on an aerofoil in turbulent flow," *Journal of Sound and Vibration*, Vol. 542, 2023, p. 117353. https://doi.org/10.1016/J.JSV.2022.117353.

[35] Kim, J. W., Haeri, S., and Joseph, P. F., "On the reduction of aerofoil-turbulence interaction noise associated with wavy leading edges," *Journal of Fluid Mechanics*, Vol. 792, 2016, pp. 526–552. https://doi.org/10.1017/jfm.2016.95, URL https://www.cambridge.org/core/journals/journal-of-fluid-mechanics/article/on-the-reduction-of-aerofoilturbulence-interaction-noise-associated-with-wavy-leading-edges/C0D721182A270CCD490E65B34233F10E.

[36] Liu, L., Zhang, L., Wu, B., and Chen, B., "Numerical and experimental studies on grid-generated turbulence in wind tunnel," *Journal of Engineering Science and Technology Review*, Vol. 10, No. 3, 2017, pp. 159–169. https://doi.org/10.25103/jestr.103.21, URL www.jestr.org.

[37] Djenidi, L., "Lattice-Boltzmann simulation of grid-generated turbulence," *Journal of Fluid Mechanics*, Vol. 552, 2006, pp. 13–35. https://doi.org/10.1017/S002211200600869X, URL https://doi.org/10.1017/S002211200600869Xhttps://www.cambridge.org/core/journals/journal-of-fluid-mechanics/article/latticeboltzmann-simulation-of-gridgenerated-turbulence/38BC72FCCE7BB2993B944286EED2E01C.

[38] Torrano, I., Tutar, M., Martinez-Agirre, M., Rouquier, A., Mordant, N., and Bourgoin, M., "Comparison of experimental and RANS-based numerical studies of the decay of grid-generated turbulence," *Journal of Fluids Engineering, Transactions of the ASME*, Vol. 137, No. 6, 2015. https://doi.org/10.1115/1.4029726, URL https://asmedigitalcollection.asme.org/fluidsengineering/article/137/6/061203/371864/Comparison-of-Experimental-and-RANS-Based.

[39] Ertunç, , Özyilmaz, N., Lienhart, H., Durst, F., and Beronov, K., "Homogeneity of turbulence generated by static-grid structures," *Journal of Fluid Mechanics*, Vol. 654, 2010, pp. 473–500. https://doi.org/10.1017/S0022112010000479, URL https://www.cambridge.org/core/journals/journal-of-fluid-mechanics/article/homogeneity-of-turbulence-generated-by-staticgrid-structures/4BBADFA0A25C54AC384F0A16DA48BEEFhttps://doi.org/10.1017/S0022112010000479.

[40] Djenidi, L., and Tardu, S. F., "On the anisotropy of a low-Reynolds-number grid turbulence," *Journal of Fluid Mechanics*, Vol. 702, 2012, pp. 332–353. https://doi.org/10.1017/jfm.2012.179, URL https://www.cambridge.org/core/journals/journal-of-fluid-mechanics/article/on-the-anisotropy-of-a-lowreynoldsnumber-grid-turbulence/A478DDE62FDA797D7ED00267083905CF.

[41] Djenidi, L., Tardu, S. F., and Antonia, R. A., "Relationship between temporal and spatial averages in grid turbulence," *Journal of Fluid Mechanics*, Vol. 730, 2013, pp. 593–606. https://doi.org/10.1017/jfm.2013.351, URL https://www.cambridge.org/core/journals/journal-of-fluid-mechanics/article/relationship-between-temporal-and-spatial-averages-in-grid-turbulence/6CEF72EE850CDE1773072518A3B8F89B.

[42] Olivieri, S., Viola, F., Mazzino, A., and Rosti, M. E., "Direct numerical simulation of flapping flags in grid-induced turbulence," *Physics of Fluids*, Vol. 33, No. 8, 2021, p. 085116. https://doi.org/10.1063/5.0060181, URL https://doi.org/10.1063/5.0060181https://aip.scitation.org/doi/abs/10.1063/5.0060181.

[43] Wu, J., Yangzhou, J., Ma, Z., and Huang, X., "Numerical study of rotor unsteady forces and noise due to ingestion of grid-generated turbulence," *Physics of Fluids*, Vol. 35, No. 1, 2023, p. 015141. https://doi.org/10.1063/5.0132975, URL https://aip.scitation.org/doi/abs/10.1063/5.0132975.

[44] Casalino, D., Grande, E., Romani, G., Ragni, D., and Avallone, F., "Definition of a benchmark for low Reynolds number propeller aeroacoustics," *Aerospace Science and Technology*, Vol. 113, 2021, p. 106707. https://doi.org/10.1016/j.ast.2021.106707, URL https://doi.org/10.1016/j.ast.2021.106707.

[45] Casalino, D., Ribeiro, A. F., Fares, E., and Nölting, S., "Lattice-Boltzmann aeroacoustic analysis of the LAGOON landing-gear configuration," *AIAA Journal*, Vol. 52, No. 6, 2014, pp. 1232–1248. https://doi.org/10.2514/1.J052365.

[46] Gonzalez-Martino, I., Wang, J., Romani, G., and Casalino, D., "Rotor noise generation in a turbulent wake using the lattice-boltzmann method," *2018 AIAA/CEAS Aeroacoustics Conference*, 2018. https://doi.org/10.2514/6.2018-3447.

[47] Casalino, D., Romani, G., Zhang, R., and Chen, H., "Lattice-Boltzmann Calculations of Rotor Aeroacoustics in Transitional Boundary Layer Regime," *28th AIAA/CEAS Aeroacoustics 2022 Conference*, 2022. https://doi.org/10.2514/6.2022-2862, URL https://arc.aiaa.org/doi/10.2514/6.2022-2862.

[48] Hainaut, T., Le Garrec, T., Polacsek, C., Mincu, D. C., and Deck, S., "Aerodynamic and aeroacoustic numerical investigation of an axial fan using Lattice Boltzmann methodsglass table," *2018 AIAA/CEAS Aeroacoustics Conference*, American Institute of Aeronautics and Astronautics Inc, AIAA, 2018. https://doi.org/10.2514/6.2018-3922, URL https://arc.aiaa.org/doi/10.2514/6.2018-3922http://arc.aiaa.org.

[49] Marié, S., Ricot, D., and Sagaut, P., "Comparison between lattice Boltzmann method and Navier-Stokes high order schemes for computational aeroacoustics," *Journal of Computational Physics*, Vol. 228, No. 4, 2009, pp. 1056–1070. https://doi.org/10.1016/j.jcp.2008.10.021.

[50] Lockard, D. P., Luo, L. S., Milder, S. D., and Singer, B. A., "Evaluation of PowerFLOW for aerodynamic applications," *Journal of Statistical Physics*, Vol. 107, No. 1-2, 2002, pp. 423–478. https://doi.org/10.1023/A:1014539411062.

[51] Herrmann, D., "A Study of the Suitability of PowerFLOW as an Educational Engineering Design Tool for Undergraduate Students ." Ph.D. thesis, University of Stuttgart, 2002.

[52] Shan, X., Yuan, X. F., and Chen, H., "Kinetic theory representation of hydrodynamics: A way beyond the Navier-Stokes equation," *Journal of Fluid Mechanics*, Vol. 550, 2006, pp. 413–441. https://doi.org/10.1017/S0022112005008153, URL https://doi.org/10.1017/S0022112005008153.

[53] Chen, H., Chen, S., and Matthaeus, W. H., "Recovery of the Navier-Stokes equations using a lattice-gas Boltzmann method," *Physical Review A*, Vol. 45, No. 8, 1992, pp. 5339–5342. https://doi.org/10.1103/PhysRevA.45.R5339, URL https://journals.aps.org/pra/abstract/10.1103/PhysRevA.45.R5339.

[54] Chen, H., Kandasamy, S., Orszag, S., Shock, R., Succi, S., and Yakhot, V., "Extended Boltzmann kinetic equation for turbulent flows," *Science*, Vol. 301, No. 5633, 2003, pp. 633–636. https://doi.org/10.1126/science.1085048.

[55] Chen, H., Orszag, S. A., Staroselsky, I., and Succi, S., "Expanded analogy between Boltzmann kinetic theory of fluids and turbulence," *Journal of Fluid Mechanics*, Vol. 519, 2004, pp. 301–314. https://doi.org/10.1017/S0022112004001211.

[56] van der Velden, W. C., Casalino, D., and Romani, G., "Full-Scale Serrated Wind Turbine Trailing Edge Noise Certification Analysis Based on the Lattice-Boltzmann Method," American Institute of Aeronautics and Astronautics (AIAA), 2023. https://doi.org/10.2514/6.2023-0970, URL http://arc.aiaa.org.

[57] Casalino, D., Avallone, F., Gonzalez-Martino, I., and Ragni, D., "Aeroacoustic study of a wavy stator leading edge in a realistic fan/OGV stage," *Journal of Sound and Vibration*, Vol. 442, 2019, pp. 138–154. https://doi.org/10.1016/j.jsv.2018.10.057.

[58] Blackmore, T., Batten, W. M., and Bahaj, A. S., "Inlet grid-generated turbulence for large-eddy simulations," *International Journal of Computational Fluid Dynamics*, Vol. 27, No. 6-7, 2013, pp. 307–315. https://doi.org/10.1080/10618562.2013.819972, URL https://www.tandfonline.com/doi/abs/10.1080/10618562.2013.819972.

[59] El-Gabry, L., Thurman, D., and Poinsatte, P., "Procedure for Determining Turbulence Length Scales Using Hotwire Anemometry," *Nasa*, , No. December, 2014, p. 16. URL http://www.sti.nasa.gov.

[60] Grant, H. L., and Nisbet, I. C., "The inhomogeneity of grid turbulence," *Journal of Fluid Mechanics*, Vol. 2, No. 3, 1957, pp. 263–272. https://doi.org/10.1017/S0022112057000117, URL https://www.cambridge.org/core/journals/journal-of-fluid-mechanics/article/inhomogeneity-of-grid-turbulence/9AD82EA9242659122D7CBD511662C1F1.

[61] Bowen, L., Celik, A., and Azarpeyvand, M., "A thorough experimental investigation on aerofoil turbulence interaction noise," *Physics of Fluids*, 2023. https://doi.org/10.1063/5.0142704, URL https://aip.scitation.org/doi/10.1063/5.0142704.

[62] Romani, G., Casalino, D., and van der Velden, W., "Numerical analysis of airfoil trailing-edge noise for straight and serrated edges at incidence," *AIAA Journal*, Vol. 59, No. 7, 2021, pp. 2558–2577. https://doi.org/10.2514/1.J059457, URL https://doi.org/10.2514/1.J059457.

[63] Brès, G. A., Pérot, F., and Freed, D., "A Ffowcs Williams-Hawkings solver for lattice-boltzmann based computational aeroacoustics," *16th AIAA/CEAS Aeroacoustics Conference (31st AIAA Aeroacoustics Conference)*, American Institute of Aeronautics and Astronautics Inc., 2010. https://doi.org/10.2514/6.2010-3711, URL https://arc.aiaa.org/doi/10.2514/6.2010-3711.

[64] Casalino, D., "An advanced time approach for acoustic analogy predictions," *Journal of Sound and Vibration*, Vol. 261, No. 4, 2003, pp. 583–612. https://doi.org/10.1016/S0022-460X(02)00986-0.

[65] Van Der Velden, W. C., Casalino, D., Gopalakrishnan, P., Jammalamadaka, A., Li, Y., Zhang, R., and Chen, H., "Jet noise prediction: Validation and physical insight," *2018 AIAA/CEAS Aeroacoustics Conference*, American Institute of Aeronautics and Astronautics Inc, AIAA, 2018. https://doi.org/10.2514/6.2018-3617.

[66] Lockard, D. P., "Airframe noise predictions using the Ffowcs Williams-Hawkings equation," *International Journal of Aeroacoustics*, Vol. 21, No. 5-7, 2022, pp. 476–500. https://doi.org/10.1177/1475472X221107366, URL https://journals.sagepub.com/doi/full/10.1177/1475472X221107366.

Appendices

A. Experimental Setup

Table 2 The geometric properties of test locations in the contraction nozzle [19]

Grid Location	Height, a_G (mm)	Width, b_G (mm)	x_G (mm)	R
C	1305	1305	1040	4.4

Table 3 The geometric properties and identification of each turbulence grid, turbulence intensity, and integral length values estimated by the autocorrelation method at the position contraction nozzle exit ($x = 0$), for a free-stream velocity $U_\infty = 20\,\mathrm{m/s}$ [19]

Grid	Diameter, d (mm)	Mesh, M (mm)	σ	Turbulence intensity (%)	Integral length scale (mm)
C-1	19	75	0.45	4.8	5.9
C-2	19	100	0.35	4.9	6.1
C-3	32	167	0.35	8.1	9.4
C-4	45	233	0.35	10.1	10.8